ADVANCED MATERIALS
www.advmat.de

Real-Time and High-Resolution Bioimaging with Bright Aggregation-Induced Emission Dots in Short-Wave Infrared Region

Ji Qi, Chaowei Sun, Abudureheman Zebibula, Hequn Zhang, Ryan T. K. Kwok, Xinyuan Zhao, Wang Xi, Jacky W. Y. Lam, Jun Qian, and Ben Zhong Tang**

Fluorescence imaging in the spectral region beyond the conventional near-infrared biological window (700–900 nm) can theoretically afford high resolution and deep tissue penetration. Although some efforts have been devoted to developing a short-wave infrared (SWIR; 900–1700 nm) imaging modality in the past decade, long-wavelength biomedical imaging is still suboptimal owing to the unsatisfactory materials properties of SWIR fluorophores. Taking advantage of organic dots based on an aggregation-induced emission luminogen (AIEgen), herein microscopic vasculature imaging of brain and tumor is reported in living mice in the SWIR spectral region. The long-wavelength emission of AIE dots with certain brightness facilitates resolving brain capillaries with high spatial resolution (≈3 μm) and deep penetration (800 μm). Owning to the deep penetration depth and real-time imaging capability, in vivo SWIR microscopic angiography exhibits superior resolution in monitoring blood–brain barrier damage in mouse brain, and visualizing enhanced permeability and retention effect in tumor sites. Furthermore, the AIE dots show good biocompatibility, and no noticeable abnormalities, inflammations or lesions are observed in the main organs of the mice. This work will inspire new insights on development of advanced SWIR techniques for biomedical imaging.

Fluorescence imaging in the near-infrared (NIR) spectral region has attracted tremendous scientific interest and successfully been used in many clinical processes, due to the salient advantages of deep tissue penetration, fast imaging, clear visualization, and minimal side effect.[1–3] At present, most of the fluorescence imaging techniques are carried out within the conventional NIR biological window (NIR-I; 700–900 nm), since NIR-I fluorophores have several key features, including facilely attained materials, reasonably high quantum yield (QY) and readily available optical equipment.[4–6] However, NIR-I imaging is suboptimal as the light–tissue interactions still exist in this spectral region. An emerging imaging modality of research interest is based on the short-wave infrared (SWIR) window, i.e., 900–1700 nm.[1,7] The SWIR biomedical imaging has demonstrated much improvement compared to conventional NIR imaging by virtue of the far more

Dr. J. Qi, Dr. R. T. K. Kwok, Dr. J. W. Y. Lam, Prof. B. Z. Tang
Department of Chemistry
Hong Kong Branch of Chinese National Engineering Research Center for Tissue Restoration and Reconstruction
Division of Life Science
State Key Laboratory of Molecular Neuroscience
Institute for Advanced Study
Institute of Molecular Functional Materials
The Hong Kong University of Science and Technology
Clear Water Bay, Kowloon, Hong Kong, China
E-mail: tangbenz@ust.hk

C. Sun, H. Zhang, Prof. J. Qian
State Key Laboratory of Modern Optical Instrumentations
Centre for Optical and Electromagnetic Research
College of Optical Science and Engineering
Zhejiang University
Hangzhou 310058, China
E-mail: qianjun@zju.edu.cn

A. Zebibula
Department of Urology
Sir Run-Run Shaw Hospital College of Medicine
Zhejiang University
Hangzhou 310016, China

Dr. X. Zhao
Department of Occupational Medicine and Environmental Toxicology
School of Public Health
Nantong University
Nan-tong 226001, China

Prof. W. Xi
Interdisciplinary Institute of Neuroscience and Technology (ZIINT)
Zhejiang University
Hangzhou 310020, China

The ORCID identification number(s) for the author(s) of this article can be found under https://doi.org/10.1002/adma.201706856.

DOI: 10.1002/adma.201706856

reduced light scattering, less tissue autofluorescence, deeper tissue penetration, and higher spatial resolution.[8–10] Nevertheless, current SWIR fluorescence imaging techniques still more or less suffer from several serious problems, for example, low QY, potential toxicity, and unoptimized imaging system, which limit their applications for advanced medical diagnosis/clinical translation.[11–13]

Nanostructured materials (e.g., quantum dots,[14,15] carbon nanotubes (CNTs),[16,17] rare-earth doped nanoparticles (NPs),[18,19] and organic/polymer NPs[20,21]) are promising contrast agents for bioimaging of whole body, main organs, and diseases such as tumors through the enhanced permeability and retention (EPR) effect passively.[22,23] Among them, the organic fluorophores doped NPs are considered to be of great potential for in vivo imaging, which possess some intrinsic merits of tunable chemical structures, easy processibility, and good biocompatibility.[24,25] Currently, the maximal emission of organic fluorophores has been extended to longer than 1200 nm, but the fluorescence QY usually does not exceed 2% in aqueous dispersion/solution, which raises harsh request for the sensitivity and imaging speed of optical detectors during in vivo imaging.[26,27] The emission wavelength and fluorescence efficiency of organic chromophores seem contrary to or work against each other due to the dominated nonradiative decay in low-bandgap materials.[28,29] A possible solution is to make fully use of the bright NIR-I emitters with strong emission in SWIR region, which would combine the material advantages of NIR-I fluorophores (e.g., high QY) and optical merits of SWIR window (e.g., less scattering and autofluorescence). Another issue that disturbs conventional organic fluorophores is the aggregation-caused quenching effect, which leads to weak or nearly no emission in aggregate state and seriously hampers their biological applications.[30] The recently developed aggregation-induced emission luminogens (AIEgens) are promising candidates for biomedical imaging, especially in nanoparticle form, as the brightness of AIE dots can be enhanced by simply increasing the amount of doped AIEgens.[31–33]

In modern medical science, some severe health problems are still disturbing researchers and clinical doctors, including cancers and cardiovascular diseases.[34–36] Early-stage diagnosis and therapy of these diseases based on angiographic imaging is significantly important to increase the recovery rate. Angiographic methods that provide useful information about the vascular state can be utilized to monitor vascular changes during disease process including vasculature, hemodynamics, thrombus, and pathologic region.[37,38] However, current imaging methods for vasculature and hemodynamics in small vessels in vivo are far less than satisfied. For example, computed tomography and magnetic resonance imaging can only resolve features down to 100 μm, and they are also limited by the long-time scanning, complex posttreatment, and difficulty in recording the vascular hemodynamics.[39,40] Fluorescence microscopic imaging would be a better choice to tackle these problems, and achieve visualization of the blood vessels in deep tissue with high temporal and spatial resolution.[41,42]

Herein, we report an NIR AIEgen (**TQ-BPN**, **Figure 1**a) and its application for in vivo functional bioimaging in SWIR region. The encapsulated **TQ-BPN** dots could emit light in a broad range of 700–1200 nm with a high QY of 13.9%, and the QY in SWIR region (>900 nm) also reached 2.8%, which was better than some typically used SWIR emitters, e.g., CNTs (≈0.4%). In vivo SWIR fluorescence microscopic imaging of mouse brain with the AIE dots enabled us to directly visualize the brain vasculature in high temporal (25 frames per second) and spatial (2.6 μm) resolution, as well as a depth of 800 μm. This represented one of the best results of SWIR fluorescence imaging, considering temporal, spatial, and deep scales together. The SWIR fluorescence microscopy assisted with bright AIE dots also allowed of assessing vascular hemodynamics, and precisely monitoring photothrombotic ischemia (PTI) and blood–brain barrier (BBB) damage in mouse brain. Interestingly, the EPR effect could be in situ visualized in tumor-bearing mice, affording accurate tumor imaging and early-stage tumor detection. Moreover, **TQ-BPN** dots showed good biocompatibility, and no detectable short-term or long-term toxicity was observed.

The donor–acceptor (D–A) approach was employed to build the organic molecule, in which *N*,*N*-diphenylnaphthalen-1-amine (BPN) and thiadiazolo[3,4-*g*]quinoxaline (TQ) were used as the donor and acceptor units, respectively. Compared to the commonly used triphenylamine unit, the naphthyl group in BPN possesses the hallmark of a more twisted conformation, which would be beneficial for constructing AIE fluorophores and achieving bright AIE NPs.[43a,b] The final compound and intermediates were characterized by nuclear magnetic resonance and high-resolution mass spectra. Detailed syntheses and characterizations are presented in Scheme S1 and Figures S1–S11 in the Supporting Information. The absorption and fluorescence spectra of **TQ-BPN** in different solvents are depicted in Figure S12 (Supporting Information) and the data are summarized in Table S1 (Supporting Information). There are small changes in the absorption spectra, but noticeable solvatochromic fluorescence peaks are observed on increasing the solvent polarity. To better understand the photophysical properties, the Stokes shift ($\nu_{abs} - \nu_{em}$) versus the solvent polarity parameter (Δf) was fitted according to the Lippert–Mataga equation, which showed a good linear relationship (Figure S13, Supporting Information). Moreover, the molar absorption coefficients in various solvents varied slightly and remained at a relatively high level ($>2 \times 10^4$ cm^{-1} M^{-1}), while the fluorescence QYs decreased with increasing solvent polarity. Fluorescence QY was measured by using IR-125 as the reference (with a nominal QY of 13% in DMSO).[28] These photophysical results manifest that **TQ-BPN** molecule has the twisted intramolecular charge transfer (TICT) phenomenon.[43b,c] We then investigated the emission property of **TQ-BPN** in aggregate state by varying the water functions (f_w) in tetrahydrofuran (THF)/water mixtures (Figure 1b,c; Figure S14, Supporting Information). The fluorescence intensity decreases with the gradual addition of water into THF until $f_w = 50\%$, possibly stem from the solvent polarity effect and hence the transformation to TICT state.[28,43] The emission intensity is intensified when further increasing the water fractions (f_w) from 50 to 90%, showing typical AIE feature. The nonplanar geometry of BPN unit and free rotation of phenyl/naphthyl rings are beneficial for the AIE effect and thus efficient solid-state emission. The AIE-active molecule allows efficient solid/aggregate emission (Figure 1c; Figure S15, Supporting Information), being useful for biomedical imaging.

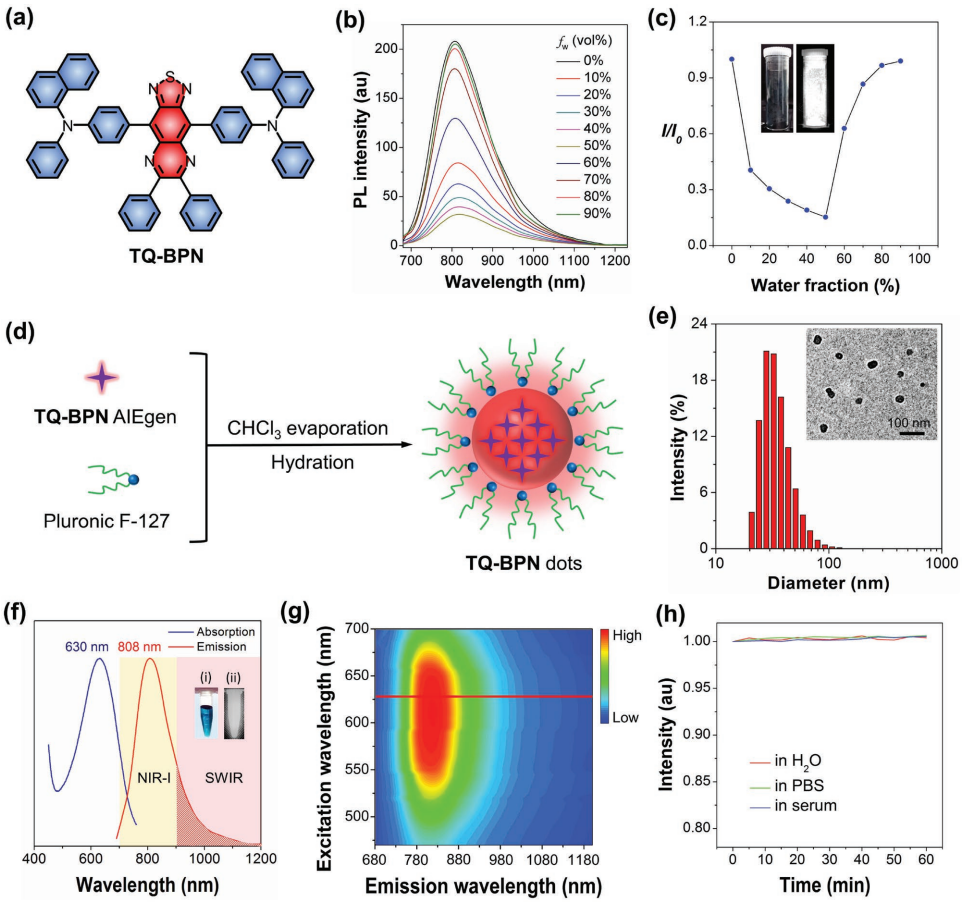

Figure 1. Characterization of **TQ-BPN** molecule and AIE dots. a) Molecular structure of **TQ-BPN**. b) Photoluminescence (PL) spectra of **TQ-BPN** in THF/H_2O mixtures with different water fractions (f_w). The concentration is 5×10^{-6} M. c) Plot of PL peak intensity of compound **TQ-BPN** versus water fraction (f_w) of THF/water mixture. I_0 and I are the PL peak intensities of the AIEgen in pure THF ($f_w = 0$) and THF/water mixtures with specific f_ws, respectively. The inset shows bright-field and SWIR fluorescence images of solid **TQ-BPN**. d) Schematic illustration of the fabrication of AIE dots. e) Representative DLS result and TEM image of the AIE dots. f) Absorption and PL spectra of **TQ-BPN** dots in water. The inset shows the photographs of (i) bright-field and (ii) SWIR images of the dots in aqueous dispersion. g) PL excitation mapping of **TQ-BPN** dots in aqueous dispersion. h) Photostability curves of the AIE dots in water, PBS, and serum under continuous 635 nm laser irradiation (1 mW cm^{-2}).

To endow biocompatibility and water dispersity to the AIEgen, we encapsulated **TQ-BPN** into organic dots in the assistance of FDA-approved amphiphilic polymer of poly(ethylene oxide)–poly(propylene oxide)–poly(ethylene oxide) (Pluronic F-127) (Figure 1d). The morphology and photophysical property of **TQ-BPN** AIE dots were studied. Transmission electron microscopy (TEM) image reveals uniform sphere structure with a diameter of about 33 nm, which matches well with the dynamic light scattering (DLS) measurement (Figure 1e). The UV–vis absorption and NIR fluorescence spectra of **TQ-BPN** dots (Figure 1f) are similar with the solution-state profiles (Figure S12, Supporting Information). Photoluminescence (PL) excitation mapping was carried out to gain in-depth understanding about the excitation–fluorescence relationships of **TQ-BPN** dots, in which an excitation/emission peak at ≈630/810 nm and an intense tail to 1200 nm were observed (Figure 1g). The AIE dots exhibited good photostability when suspended in water, phosphate buffer saline (PBS), and serum, and no noticeable decrease in emission intensity was observed after continuous 635 nm laser irradiation (the same light source used for in vivo imaging) for 1 h (Figure 1h; Figure S16, Supporting Information). It is worth mentioning that the photostability of the AIE dots is much better than the widely used methylene blue (Figure S17, Supporting Information). The QY of AIE dots was measured to be 13.9% in the whole emission spectrum, and the fluorescence in SWIR region (>900 nm) had a QY of 2.8% (Figure S18, Supporting Information), which was higher than some typical SWIR fluorophores, e.g., CNTs (≈0.4%) and organic emitters (0–2%).[8,29] These results suggest that although **TQ-BPN** exhibits an emission peak at ≈810 nm, it could also be used for SWIR fluorescence imaging because of the high fluorescence efficiency and broad emission range.

To glean the difference between the spectral regions below and within SWIR region, we imaged the same mouse treated with **TQ-BPN** dots using a silicon-based CCD camera in the spectral region <900 nm and an InGaAs camera in SWIR region, respectively. Interestingly, an obvious distinction in image quality was observed in these two spectral regions. Compared to NIR-I mode (Figure S19, Supporting Information), the SWIR imaging gives much higher resolution (**Figure 2**a),

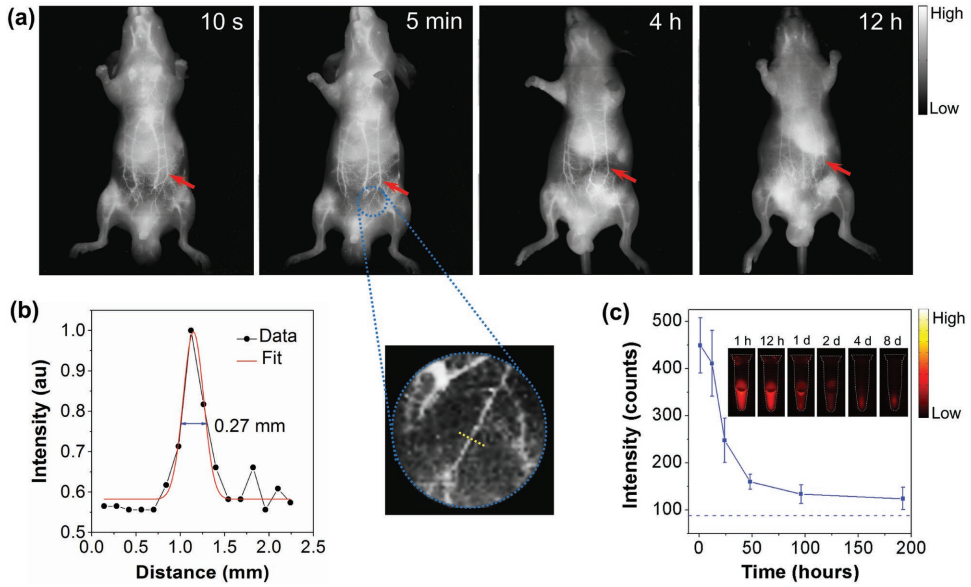

Figure 2. Long-term SWIR fluorescence whole-body imaging of living mice. a) SWIR images of the mouse treated with **TQ-BPN** dots at various time points (10 s, 5 min, 4 h, and 12 h) under 635 nm excitation (1 mW cm^{-2}). The red arrows show the blood vessels. b) A cross-sectional fluorescence intensity profiles along yellow-dashed lines of the mice injected with **TQ-BPN** dots. Gaussian fits to the profile are shown in red line. c) Time-dependent SWIR fluorescence intensity of the blood extracted from the AIE-dots treated mice at different time points. The dashed blue line indicates the fluorescence intensity of blood from the mice without any treatment (control). The inset shows SWIR fluorescence images of the blood at different time points as indicated.

suggesting that SWIR light could provide better in vivo imaging clarity. It should be noted that the capillary with a small diameter of about 0.27 mm could be unambiguously detected (Figure 2b). Next, we performed long-term SWIR whole-body imaging (all the fluorescence imaging below was carried out within SWIR region unless noted) of healthy mice after intravenous injection of AIE dots, and the mice were then imaged with InGaAs camera under 635 nm laser (1 mW cm^{-2}) excitation. As shown in Figure 2a, the blood vessels could be clearly discriminated even 12 h posttreatment, indicating that the AIE dots were useful for long-term angiography, probably because that the long PEG chains of F-127 could prolong the circulation time of AIE dots in mouse blood.[44,45] Time-dependent monitoring of the SWIR fluorescence intensity of the blood extracted from the **TQ-BPN** dots treated mice also confirmed the long-time retention characteristic (Figure 2c). A clear visualization of a mouse in different positions is shown in Movie S1 and Figure S20 in the Supporting Information. It could be concluded from these results that the organic dots were mainly captured and concentrated by the reticuloendothelial system organs including liver and spleen, and profiled them gradually.[24]

In order to enable more precise tracking of tiny vessels, we performed microscopic angiography of mouse brain. An SWIR fluorescence wide-field microscope was set up, in which a 635 nm laser diode was utilized as the excitation source. The microscopic imaging system combines the benefits of video-rate imaging capability of traditional wide-field fluorescence microscopy and deep tissue penetration of SWIR fluorescence signals (Figure S21, Supporting Information). Five minutes after the injection of **TQ-BPN** dots into an institute of cancer research (ICR) mouse through tail vein, in vivo imaging on the mouse brain was implemented by tuning focus plane gradually to increase the imaging depth. **Figure 3** shows the representative fluorescence images of mouse brain at various vertical depths below skull. The blood vasculature in mouse brain can be finely visualized at various imaging depths, which helps to reconstruct the 3D vasculature architecture. It is interesting to note that tiny structure of capillary vessels (diameter = 18.4 μm) can still be distinguished at the depth of 800 μm (the red arrows in Figure 3), which is one of the best SWIR microscopic imaging results in terms of imaging depth and resolution.[9] To understand the circulation time of **TQ-BPN** dots in blood, long-term microscopic brain angiography was also carried out. As presented in Figure S22 (Supporting Information), the fluorescence signals in brain blood vessels could be detected even at 120 h postinjection (p.i.), revealing that the circulation time of **TQ-BPN** dots was more than 5 d. Assisted by the bright emission and biocompatible PEG chains of the AIE dots, SWIR fluorescence microscopy enables high-resolution, deep-tissue and long-term vascular structure observation, and blood flow tracking in vivo.

Next, we performed noninvasive SWIR imaging of blood vessels at different positions in the brain of living mice. Owing to the bright fluorescence from the AIE dots, a high spatial resolution of 2.6 μm and a large signal-to-noise ratio (S/N) of 33 at the depth of 150 μm in mouse brain are realized, which are among the best resolution attained by SWIR fluorescence imaging (**Figure 4**a,b).[16] In order to evaluate the hemodynamic characteristic in vivo, a small point signal in the blood capillary was tracked (Figure 4c; Movie S2, Supporting Information). As shown in Figure 4d, the position of this point as a function of time was plotted, giving an average blood velocity of 161.8 μm s^{-1} in the fine blood capillary (diameter = 4.4 μm). In addition, we also tracked a point signal in another thick blood capillary (diameter = 56.5 μm), and obtained an average blood velocity

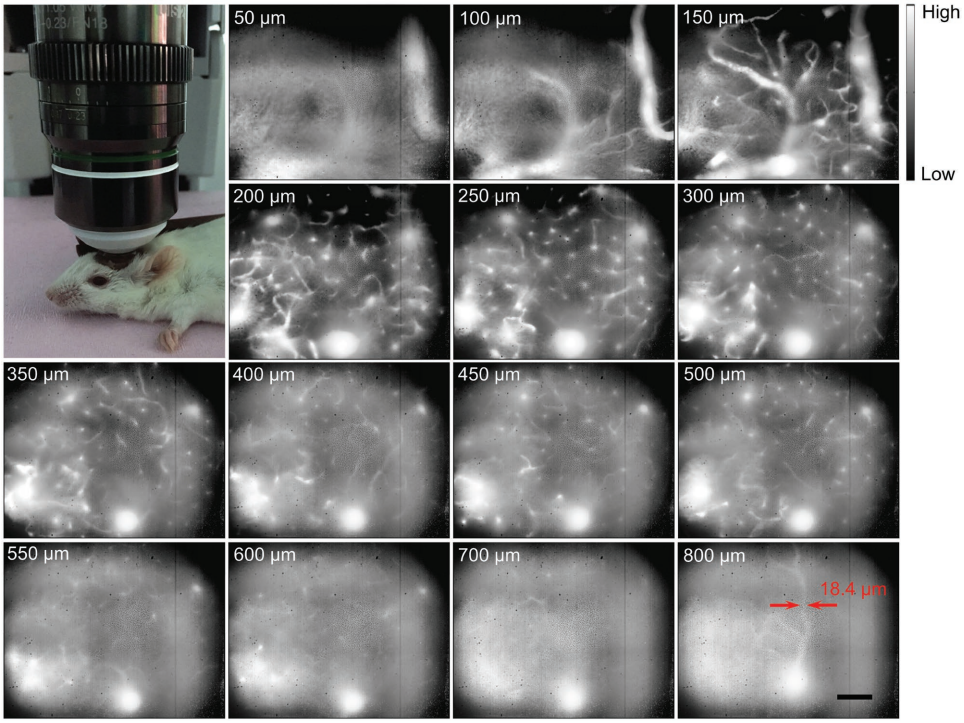

Figure 3. In vivo and real-time SWIR fluorescence microscopic imaging of mouse brain vasculature at various depths (50–800 μm) after intravenous injection of **TQ-BPN** dots. λ_{ex} = 635 nm. The red arrows show the tiny blood capillary observed at the depth of 800 μm (diameter = 18.4 μm). The scale bar indicates 100 μm.

of 918.57 μm s^{-1}, which allowed us to evaluate the volume blood flow of 0.553 μL min^{-1} (Figure S23 and Movie S3, Supporting Information). These results illustrate that the blood velocity is diverse in different vessels, and faster in thick blood capillary.[46] According to the spatial resolution (1 μm), field of view (633 μm × 506 μm) and frame rate (25 frames per second) of the SWIR fluorescence microscopy, the dynamic range of blood velocity detection could be calculated in the range of 25–20 000 μm s^{-1}, nearly covering all the vascular flowing speeds in mouse brain.[46,47]

To further explore the potential applications of **TQ-BPN** dots in disease diagnostics, we monitored PTI induction in mouse brain using in vivo SWIR microscopic angiography. As well known, PTI in brain may induce the damage of BBB. BBB is a specialized cerebral vascular system that strictly controls the transport of blood–borne substances into brain.[48,49] Thus, developing a feasible imaging technology for real-time and accurate monitoring of PTI and BBB damage in deep brain is of great significance. The schematic of PTI induction process in blood vasculature is presented in Figure 4e. The SWIR fluorescence microscope was slightly modulated for the brain PTI induction and real-time imaging simultaneously (Figure S24, Supporting Information). A 1040 nm femtosecond (fs) laser beam was employed as the excitation source for PTI induction, and a photomultiplier-tube-based scanning imaging system was used as the guidance. The intravenously injected photosensitizer (rose bengal) in brain blood vessels could release singlet oxygen ($^1O_2$) under the two-photon excitation of 1040 nm fs laser, then $^1O_2$ adhered to the endothelial cells of blood vessels and destroyed them.[25] Subsequently, blood platelets would gather in the destroyed regions to repair them and thus cause blocking, which is a kind of cerebral thrombosis. Figure 4f shows the selected cortical vessel before and after PTI formation, in which the dashed boxes indicate the region excited by 1040 nm fs laser for 30 s. The blood flow was apparently blocked at the injured area, since the fluorescence signals nearby (the two green arrows in blood vessel in Figure 4f) abnormally increased as a result of **TQ-BPN** dots accumulation. A video imaging result of this process is shown in Movie S4 (Supporting Information), which obviously reveals the PTI-caused partial cerebral thrombosis. Furthermore, we introduced more serious PTI by exciting brain blood vessel for 3 min. As shown in Figure S25 and Movie S5 in the Supporting Information, a big bubble appeared, and the **TQ-BPN** dots leaked out from the blood vessels, illustrating BBB damage in serious PTI site. These results suggest that the AIE-dot-based SWIR imaging technique could facilitate real-time tracking of thrombotic ischemia in mouse brain, and may allow in situ probing the pathogenesis of brain diseases.

Early-stage detection and treatment of tumors are critically important, because they can efficiently improve the recovery rate.[50] Currently, monitoring early-stage tumors and cancer metastases are still facing great challenges with traditional radiography approaches. As demonstrated above, the **TQ-BPN**-dot-based SWIR imaging could achieve deep-tissue, real-time, and high-resolution visualization of biological samples in both whole-body and microscopic modes, which encouraged us to test its feasibility for precise cancer detection and differentiation. At first, a nude mouse with subcutaneously xenografted tumors (two weeks) was injected with **TQ-BPN** dots via tail vein, and the

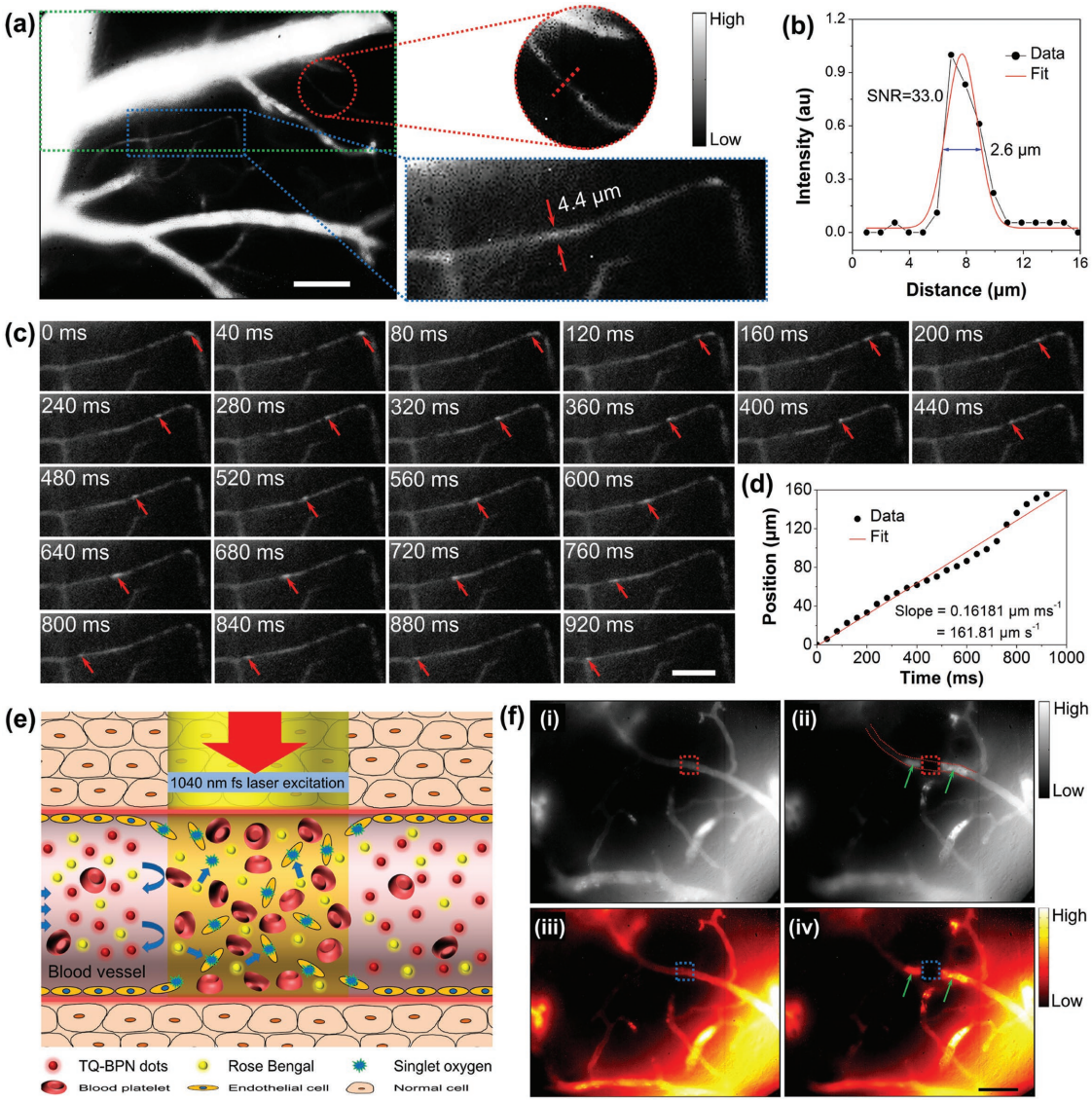

Figure 4. SWIR fluorescence microscopic imaging of hemodynamics study and real-time tracking of thrombotic ischemia in mouse brain. a) A microscopic image of brain vasculature. Depth = 150 μm. b) A cross-sectional fluorescence intensity profile (black) and a Gaussian fit (red) along the red-dashed bar in the red-dashed circle of (a). c) A time course of the point signal randomly tracked in a blood capillary (diameter = 4.4 μm) in the blue-dashed box of (a). d) Plot of the position of a point signal as a function of time. e) Schematic illustration of PTI induction under two-photon excitation. f) SWIR fluorescence microscopic images of brain blood vessels before (i) and after (ii) PTI induction. (iii) and (iv) are the heat maps of (i) and (ii), respectively. Red and blue dashed boxes stand for the 1040 nm fs laser excited regions. The scale bars in (a) and (f) indicate 100 μm, and the scale bar in (c) indicates 50 μm.

accumulation of organic dots on tumors was clearly observed 24 h posttreatment (Figure S26, Supporting Information). We next attempted to utilize SWIR fluorescence microscopy to identify the tumors at different growing stages. A mouse with an old tumor (four weeks) and a new tumor (two weeks) was treated with **TQ-BPN** dots, and observed under the SWIR fluorescence microscopic system (**Figure 5**a,b) immediately (5 min) and 24 h after intravenous injection, respectively. As shown in Figure 5d, both the old and new tumors were not well distinguished 5 min p.i. However, the blood vessels (depth = 180 μm) of both the old and new tumors were clearly visualized, and nearly no fluorescence signals could be detected outside the blood vessels. After 24 h, the old tumor was still not well resolved, whereas the new tumor was markedly visualized (Figure 5d). It is noted that there were a lot of fluorescence aggregates outside the vessels of the new tumor, in obvious contrast to the case in the old one. We also studied other regions of the old and new tumors, and similar results were observed (Figure S27, Supporting Information). The experimental results could be explained by the EPR effect. As presented in Figure 5c, new tumor grows faster than old tumor and normal tissues, thus a lot of newly grown vessels are formed in tumor region to supply nutrition and oxygen. However, these new vessels composed of poorly aligned defective endothelial cells are usually in abnormal form and architecture, i.e., wide fenestrations. Accordingly, the AIE dots can diffuse from the blood vessels to extravascular tissues,

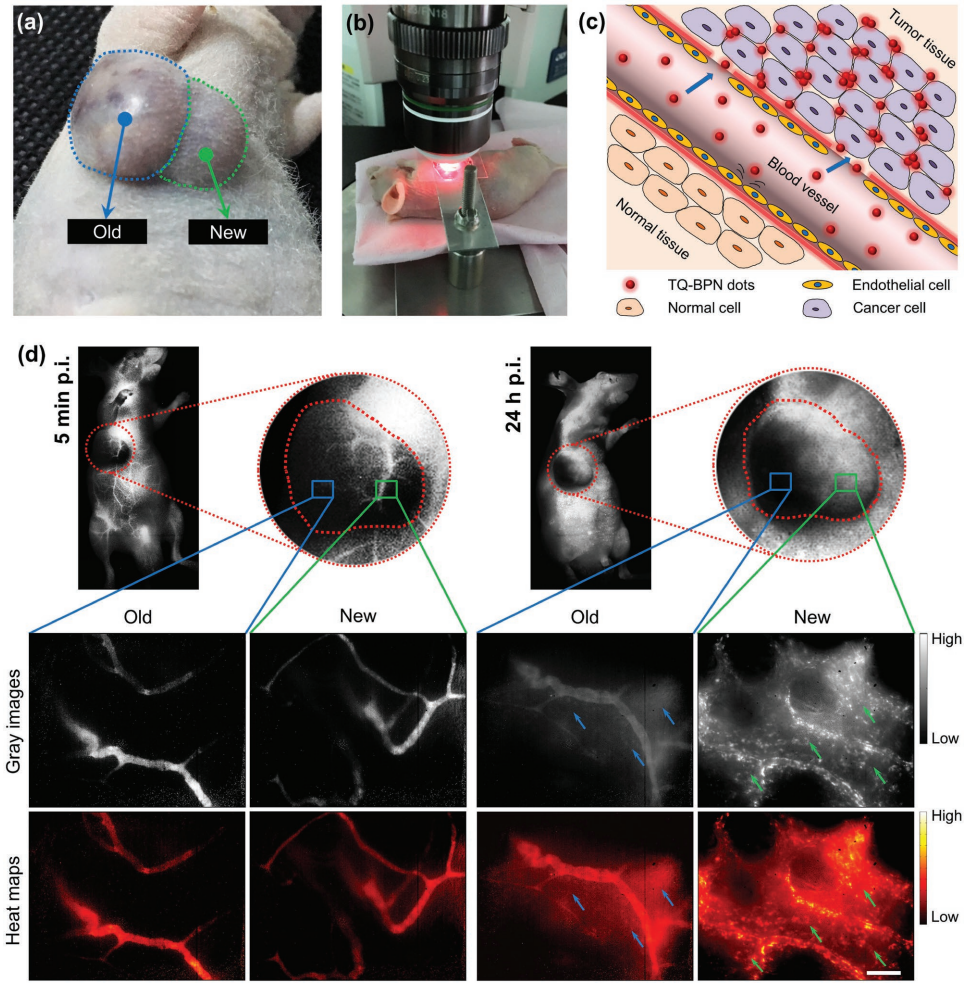

Figure 5. In situ visualization of the enhanced permeability and retention (EPR) effect in tumor sites with SWIR fluorescence imaging. a) The photograph of a tumor-bearing mouse used for in vivo microscopic imaging. The left is an old tumor and the right is a new tumor. b) A photograph showing the microscopic imaging on tumor sites. c) Schematic illustration of the EPR effect. d) SWIR fluorescence microscopic imaging for visualizing EPR effect in the old and new tumors at different time points. Depth = 180 µm. The scale bar indicates 100 µm.

aggregate, and result in brighter fluorescent spots. The SWIR fluorescence microscopy enabled clear in situ visualization of EPR effect in tumor sites, which would be beneficial for early-stage tumor detection and metastasis investigation.[51]

Biocompatibility is critical for fluorescent labels, so we evaluated the biosafety of the AIE dots.[11,52] We first tested the relative viability of the **TQ-BPN** dots treated cells (Figure S28, Supporting Information), and it showed no distinct decrease at a high concentration of 100 µg mL^{-1} (based on **TQ-BPN** molecule). We then carried out the study of the relative mortality rate, relative malformation rate, cumulative hatching rate, and relative gene expression level on zebrafish (Figure S29, Supporting Information) after the treatment with AIE dots, it also showed no detectable toxicity to zebrafish. Moreover, we evaluated the toxicity of **TQ-BPN** dots in mice via histological study. The hematoxylin and eosin stain (Figure S30, Supporting Information) revealed that no noticeable short-term (2 h p.i.) and long-term (48 d p.i.) damage or inflammatory lesion could be observed in major organs of the mice. Finally, we performed the hepatic/renal function analysis and blood routine examination of the AIE dots treated mice, where no hepatotoxicity, nephrotoxicity or hematological toxicity was observed (Figures S31 and S32, Supporting Information). Taken together, our results illustrate that **TQ-BPN** dots possess good biocompatibility, and therefore could be used for in vivo bioimaging.

In summary, we have developed a kind of NIR AIE dots for real-time and high-resolution imaging in living mice in SWIR spectral region. Noteworthy, although **TQ-BPN** dots exhibit maximal emission at ≈810 nm, owning to the high fluorescence QY (13.9%) and long emission tail to 1200 nm, the partial emission with QY of 2.8% in SWIR region (>900 nm) is sufficient to enable SWIR fluorescence imaging. We also developed macro and microfluorescence imaging systems, which could be effectively used for whole-body screening and microscopic imaging of main organs/diseases. By virtue of the bright AIE dots and SWIR macro imaging system, we have resolved the blood capillaries of mouse brain with a high spatial resolution of sub 3 µm at a depth of 150 µm, and the tiny structure of capillary vessels can also be clearly discriminated at the depth of 800 µm, which is among the best resolution for in vivo fluorescence imaging

of mouse brain. In vivo and real-time microscopic angiography based on SWIR imaging was further used to investigate PTI induction and BBB damage in mouse brain, suggesting a facile method to dynamically evaluate vascular diseases. Interestingly, the AIE dots are also a versatile tool capable of visualizing EPR effect and detecting early-stage tumor in situ, which is critical for fundamental understanding and tumor diagnosis/therapy. The current work enables real-time, deep-tissue, high-resolution, and long-term in vivo angiography, rendering great promise for disease diagnostics. This work will inspire new insights on development of advanced SWIR fluorescence techniques for biomedical imaging.

Experimental Section

The detailed experimental process is available in the Supporting Information.

Supporting Information

Supporting Information is available from the Wiley Online Library or from the author.

Acknowledgements

J.Q. and C.S. contributed equally to this work. This work was supported by the National Basic Research Program of China (973 Program; 2013CB834701 and 2013CB834704), the National Natural Science Foundation of China (Grant No. 61275190), the Zhejiang Provincial Natural Science Foundation of China (Grant No. LR17F050001), the University Grants Committee of Hong Kong (AoE/P-03/08), the Research Grants Council of Hong Kong (Grant Nos. 16305015, 16308016, and N-HKUST604/14), the Innovation and Technology Commission (Grant Nos. ITC-CNERC14SC01 and ITCPD117-9), and the Science and Technology Plan of Shenzhen (Grant No. JCYJ20160229205601482).

Conflict of Interest

The authors declare no conflict of interest.

Keywords

aggregation-induced emission, blood–brain barrier, cancer, deep brain penetration

Received: November 23, 2017
Revised: December 20, 2017
Published online: January 17, 2018

[1] G. Hong, A. L. Antaris, H. Dai, *Nat. Biomed. Eng.* **2017**, *1*, 0010.
[2] J. F. Lovell, C. S. Jin, E. Huynh, H. Jin, C. Kim, J. L. Rubinstein, W. C. Chan, W. Cao, L. V. Wang, G. Zheng, *Nat. Mater.* **2011**, *10*, 324.
[3] W. Shao, G. Chen, A. Kuzmin, H. L. Kutscher, A. Pliss, T. Y. Ohulchanskyy, P. N. Prasad, *J. Am. Chem. Soc.* **2016**, *138*, 16192.
[4] Q. Miao, C. Xie, X. Zhen, Y. Lyu, H. Duan, X. Liu, J. V. Jokerst, K. Pu, *Nat. Biotechnol.* **2017**, *35*, 1102.
[5] S. Lu, L. Sui, J. Liu, S. Zhu, A. Chen, M. Jin, B. Yang, *Adv. Mater.* **2017**, *29*, 1603443.
[6] W. Li, J. Wang, J. Ren, X. Qu, *J. Am. Chem. Soc.* **2014**, *136*, 2248.
[7] E. Hemmer, A. Benayas, F. Légaré, F. Vetrone, *Nanoscale Horiz.* **2016**, *1*, 168.
[8] A. L. Antaris, H. Chen, K. Cheng, Y. Sun, G. Hong, C. Qu, S. Diao, Z. Deng, X. Hu, B. Zhang, X. Zhang, O. K. Yaghi, Z. R. Alamparambil, X. Hong, Z. Cheng, H. Dai, *Nat. Mater.* **2016**, *15*, 235.
[9] O. T. Bruns, T. S. Bischof, D. K. Harris, D. Franke, Y. Shi, L. Riedemann, A. Bartelt, F. B. Jaworski, J. A. Carr, C. J. Rowlands, M. W. B. Wilson, O. Chen, H. Wei, G. W. Hwang, D. M. Montana, I. Coropceanu, O. B. Achorn, J. Kloepper, J. Heeren, P. T. C. So, D. Fukumura, K. F. Jensen, R. K. Jain, M. G. Bawendi, *Nat. Biomed. Eng.* **2017**, *1*, 0056.
[10] C. Li, F. Li, Y. Zhang, W. Zhang, X. E. Zhang, Q. Wang, *ACS Nano* **2015**, *9*, 12255.
[11] L. Cheng, W. He, H. Gong, C. Wang, Q. Chen, Z. Cheng, Z. Liu, *Adv. Funct. Mater.* **2013**, *23*, 5893.
[12] E. Oh, R. Liu, A. Nel, K. B. Gemill, M. Bilal, Y. Cohen, I. L. Medintz, *Nat. Nanotechnol.* **2016**, *11*, 479.
[13] A. M. Smith, M. C. Mancini, S. Nie, *Nat. Nanotechnol.* **2009**, *4*, 710.
[14] C. Li, Y. Zhang, G. Chen, F. Hu, K. Zhao, Q. Wang, *Adv. Mater.* **2017**, *29*, 1605754.
[15] L. Jing, S. V. Kershaw, Y. Li, X. Huang, Y. Li, A. L. Rogach, M. Gao, *Chem. Rev.* **2016**, *116*, 10623.
[16] K. Welsher, Z. Liu, S. P. Sherlock, J. T. Robinson, Z. Chen, D. Daranciang, H. Dai, *Nat. Nanotechnol.* **2009**, *4*, 773.
[17] C. Liang, S. Diao, C. Wang, H. Gong, T. Liu, G. Hong, X. Shi, H. Dai, Z. Liu, *Adv. Mater.* **2014**, *26*, 5646.
[18] G. Chen, H. Qiu, P. N. Prasad, X. Chen, *Chem. Rev.* **2014**, *114*, 5161.
[19] Z. Gu, L. Yan, G. Tian, S. Li, Z. Chai, Y. Zhao, *Adv. Mater.* **2013**, *25*, 3758.
[20] D. Li, W. Qin, B. Xu, J. Qian, B. Z. Tang, *Adv. Mater.* **2017**, *29*, 1703643.
[21] K. Li, B. Liu, *Chem. Soc. Rev.* **2014**, *43*, 6570.
[22] X. Zhen, Y. Tao, Z. An, P. Chen, C. Xu, R. Chen, W. Huang, K. Pu, *Adv. Mater.* **2017**, *29*, 1606665.
[23] X. Ai, C. J. H. Ho, J. Aw, A. B. E. Attia, J. Mu, Y. Wang, X. Wang, Y. Wang, X. Liu, H. Chen, M. Gao, X. Chen, E. K. L. Yeow, G. Liu, M. Olivo, B. Xing, *Nat. Commun.* **2016**, *7*, 10432.
[24] J. Qi, Y. Fang, R. T. K. Kwok, X. Zhang, X. Hu, J. W. Y. Lam, D. Ding, B. Z. Tang, *ACS Nano* **2017**, *11*, 7177.
[25] W. Wu, D. Mao, F. Hu, S. Xu, C. Chen, C.-J. Zhang, X. Cheng, Y. Yuan, D. Ding, D. Kong, B. Liu, *Adv. Mater.* **2017**, *29*, 1700548.
[26] Q. Yang, Z. Ma, H. Wang, B. Zhou, S. Zhu, Y. Zhong, J. Wang, H. Wan, A. Antaris, R. Ma, X. Zhang, J. Yang, X. Zhang, H. Sun, W. Liu, Y. Liang, H. Dai, *Adv. Mater.* **2017**, *29*, 1605497.
[27] Y. Sun, C. Qu, H. Chen, M. He, C. Tang, K. Shou, S. Hong, M. Yang, Y. Jiang, B. Ding, Y. Xiao, L. Xing, X. Hong, Z. Cheng, *Chem. Sci.* **2016**, *7*, 6203.
[28] X. Du, J. Qi, Z. Zhang, D. Ma, Z. Y. Wang, *Chem. Mater.* **2012**, *24*, 2178.
[29] G. Qian, J. Qi, J. A. Davey, J. S. Wright, Z. Y. Wang, *Chem. Mater.* **2012**, *24*, 2364.
[30] J. B. Birks, *Photophysics of Aromatic Molecules*, Wiley, London, UK **1970**.
[31] J. Mei, N. L. Leung, R. T. Kwok, J. W. Lam, B. Z. Tang, *Chem. Rev.* **2015**, *115*, 11718.
[32] D. Ding, K. Li, B. Liu, B. Z. Tang, *Acc. Chem. Res.* **2013**, *46*, 2441.
[33] J. Qian, B. Z. Tang, *Chem* **2017**, *3*, 56.
[34] K. Pu, A. J. Shuhendler, J. V. Jokerst, J. Mei, S. S. Gambhir, Z. Bao, J. Rao, *Nat. Nanotechnol.* **2014**, *9*, 233.

[35] G. Lv, W. Guo, W. Zhang, T. Zhang, S. Li, S. Chen, A. S. Eltahan, D. Wang, Y. Wang, J. Zhang, P. C. Wang, J. Chang, X.-J. Liang, *ACS Nano* **2016**, *10*, 9637.
[36] P. M. Ridker, N. R. Cook, *Lancet* **2013**, *382*, 1762.
[37] Y. Jia, S. T. Bailey, T. S. Hwang, S. M. McClintic, S. S. Gao, M. E. Pennesi, C. J. Flaxel, A. K. Lauer, D. J. Wilson, J. Hornegger, J. G. Fujimoto, D. Huang, *Proc. Natl. Acad. Sci. USA* **2015**, *112*, E2395.
[38] P. Loud, D. Katz, D. Bruce, D. Klippenstein, Z. Grossman, *Radiology* **2001**, *219*, 498.
[39] L. Saba, R. Sanfilippo, R. Montisci, G. Mallarini, *Neuroradiology* **2010**, *52*, 75.
[40] A. V. Naumova, M. Modo, A. Moore, C. E. Murry, J. A. Frank, *Nat. Biotechnol.* **2014**, *32*, 804.
[41] X. He, J. Gao, S. S. Gambhir, Z. Cheng, *Trends Mol. Med.* **2010**, *16*, 574.
[42] Y. Wang, H. Xiao, X. Wang, J. Li, A. W. Roe, L. Ping, J. Qian, *Adv. Healthcare Mater.* **2017**, *6*, 1700685.
[43] a) G. Qian, Z. Zhong, M. Luo, D. Yu, Z. Zhang, D. Ma, Z. Y. Wang, *J. Phys. Chem. C* **2009**, *113*, 1589; b) W. Qin, K. Li, G. Feng, M. Li, Z. Yang, B. Liu, B. Z. Tang, *Adv. Funct. Mater.* **2014**, *24*, 635; c) X. Han, Q. Bai, L. Yao, H. Liu, Y. Gao, J. Li, L. Liu, Y. Liu, X. Li, P. Lu, B. Yang, *Adv. Funct. Mater.* **2015**, *25*, 7521; d) Y. Cheng, J. Wang, Z. Qiu, X. Zheng, N. L. C. Leung, J. W. Y. Lam, B. Z. Tang, *Adv. Mater.* **2017**, *29*, 1703900.
[44] L. Rao, L.-L. Bu, J.-H. Xu, B. Cai, G.-T. Yu, X. Yu, Z. He, Q. Huang, A. Li, S.-S. Guo, W.-F. Zhang, W. Liu, Z.-J. Sun, H. Wang, T.-H. Wang, X.-Z. Zhao, *Small* **2015**, *11*, 6225.
[45] Y. Ma, S. Tong, G. Bao, C. Gao, Z. Dai, *Biomaterials* **2013**, *34*, 7706.
[46] R. P. J. Barretto, T. H. Ko, J. C. Jung, T. J. Wang, G. Capps, A. C. Waters, Y. Ziv, A. Attardo, L. Recht, M. J. Schnitzer, *Nat. Med.* **2011**, *17*, 223.
[47] G. Hong, J. C. Lee, J. T. Robinson, U. Raaz, L. Xie, N. F. Huang, J. P. Cooke, H. Dai, *Nat. Med.* **2012**, *18*, 1841.
[48] J. I. Sage, R. L. van Uitert, T. E. Duffy, *Stroke* **1984**, *15*, 46.
[49] X. Cai, A. Bandla, D. Mao, G. Feng, W. Qin, L.-D. Liao, N. Thakor, B. Z. Tang, B. Liu, *Adv. Mater.* **2016**, *28*, 8760.
[50] J. Phallen, M. Sausen, V. Adleff, A. Leal, C. Hruban, J. White, V. Anagnostou, J. Fiksel, S. Cristiano, E. Papp, S. Speir, T. Reinert, M.-B. W. Orntoft, B. D. Woodward, D. Murphy, S. Parpart-Li, D. Riley, M. Nesselbush, N. Sengamalay, A. Georgiadis, Q. K. Li, M. R. Madsen, F. V. Mortensen, J. Huiskens, C. Punt, N. van Grieken, R. Fijneman, G. Meijer, H. Husain, R. B. Scharpf, L. A. Diaz Jr., S. Jones, S. Angiuoli, T. Ørntoft, H. J. Nielsen, C. L. Andersen, V. E. Velculescu, *Sci. Transl. Med.* **2017**, *9*, eaan2415.
[51] H. Maeda, *Adv. Drug Delivery Rev.* **2015**, *91*, 3.
[52] Y. Liu, C. Chen, P. Qian, X. Lu, B. Sun, X. Zhang, L. Wang, X. Gao, H. Li, Z. Chen, J. Tang, W. Zhang, J. Dong, R. Bai, P. E. Lobie, Q. Wu, S. Liu, H. Zhang, F. Zhao, M. S. Wicha, T. Zhu, Y. Zhao, *Nat. Commun.* **2015**, *6*, 5988.

